nature nanotechnology

Article

https://doi.org/10.1038/s41565-024-01669-3

Redox-neutral electrochemical decontamination of hypersaline wastewater with high technology readiness level

Received: 15 August 2023

Accepted: 1 April 2024

Published online: 9 May 2024

Check for updates

Gong Zhang[1,6], Yongqi Li[1,2,6], Chenxuan Zhao[3,6], Jiabao Gu[1], Gang Zhou[4], Yanfeng Shi[1], Qi Zhou[1], Feng Xiao[2], Wen-jie Fu[5], Qingbai Chen[1], Qinghua Ji[1], Jiuhui Qu[1] & Huijuan Liu[1]

Industrial hypersaline wastewaters contain diverse pollutants that harm the environment. Recovering clean water, alkali and acid from these wastewaters can promote circular economy and environmental protection. However, current electrochemical and advanced oxidation processes, which rely on hydroxyl radicals to degrade organic compounds, are inefficient and energy intensive. Here we report a flow-through redox-neutral electrochemical reactor (FRER) that effectively removes organic contaminants from hypersaline wastewaters via the chlorination–dehalogenation–hydroxylation route involving radical–radical cross-coupling. Bench-scale experiments demonstrate that the FRER achieves over 75% removal of total organic carbon across various compounds, and it maintains decontamination performance for over 360 h and continuously treats real hypersaline wastewaters for two months without corrosion. Integrating the FRER with electrodialysis reduces operating costs by 63.3% and CO_2 emissions by 82.6% when compared with traditional multi-effect evaporation-crystallization techniques, placing our system at technology readiness levels of 7–8. The desalinated water, high-purity NaOH (>95%) and acid produced offset industrial production activities and thus support global sustainable development objectives.

Hypersaline wastewaters (>3.5%) arise from various industries such as chemical manufacturing, oil and gas production, and seawater desalination for potable water[1,2]. Discharge of hypersaline wastewater has a detrimental impact on aquatic ecosystems, rendering water unsuitable for direct potable use or industrial applications[3]. Currently, a significant portion of these highly saline wastewaters is treated by evaporation crystallization, which produces hazardous solid wastes and carbon dioxide[4]. According to the *China Statistical Yearbook*, around 1,500 million cubic metres of hypersaline wastewater is discharged annually and the cost of treating it is expected to exceed US$45 billion per year.

Bipolar membrane electrodialysis (BMED) emerges as an environmentally and economically sound solution, which can separate ions and recover clean water, alkali and acid from the hypersaline wastewaters[5]. Nevertheless, the presence of organic contaminants in

[1]Center for Water and Ecology, State Key Joint Laboratory of Environment Simulation and Pollution Control, School of Environment, Tsinghua University, Beijing, China. [2]School of Hydraulic and Hydropower Engineering, North China Electric Power University, Beijing, China. [3]Shanghai Key Laboratory of Magnetic Resonance, State Key Laboratory of Precision Spectroscopy, School of Physics and Electronic Science, East China Normal University, Shanghai, China. [4]Key Laboratory of Integrated Regulation and Resource Development on Shallow Lakes, Ministry of Education, College of Environment, Hohai University, Nanjing, China. [5]College of Environment and Resources, Guangxi Normal University, Guilin, China. [6]These authors contributed equally: Gong Zhang, Yongqi Li, Chenxuan Zhao. e-mail: hjliu@tsinghua.edu.cn

https://doi.org/10.1038/s41565-024-01669-3

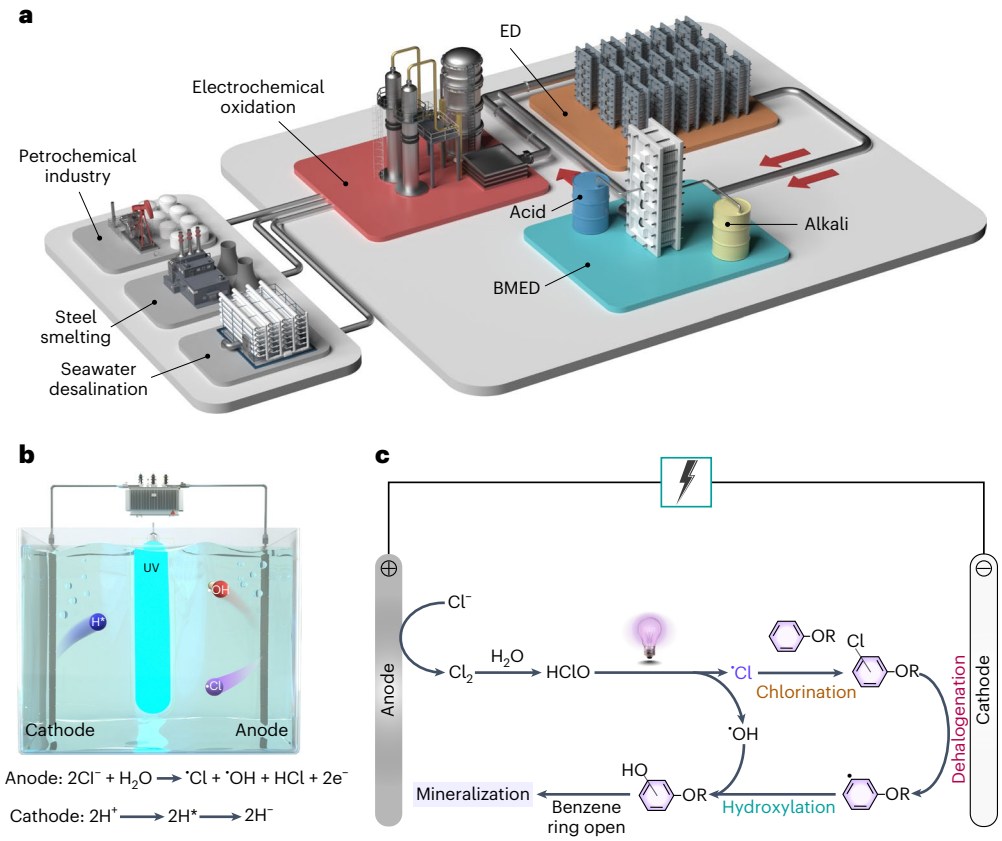

Fig. 1 | Electrochemical systems for recovering resources from hypersaline wastewaters. a, 3D illustration of an integrated electrochemical system for recovering resources from various sources of hypersaline wastewaters. The electro-oxidation plant removes organic impurities, and ED and BMED systems recover clean water, purified alkali and acid from the wastewaters. The red arrows show the flow direction. **b**, Schematic showing reactive chlorine radicals (Cl•), hydroxyl radicals (•OH) and various reductive hydrogen species in a conventional electrochemical cell for UV–chlorine treatment of wastewater. **c**, Schematic of the new CDH path for oxidizing organic impurities in hypersaline waters. The radical–radical cross-coupling •OH addition reaction in CDH bypasses the complicated •OH addition, O_2• formation and HOO• abstraction steps.

the matrix poses a challenge, by causing membrane fouling and subsequently reducing the membrane lifespan[6]. Moreover, they contribute to impurities in products that require additional treatment, thereby increasing the financial burden associated with product purification. To prevent these, it is preferable to eliminate the organic contaminants before initiating the electrodialysis (ED) process (Fig. 1a). However, traditional advanced oxidation processes such as the Fenton reaction and ozonation, usually highly adept at removing organic contaminants, lose their effectiveness when confronted with high concentrations of Cl^- in the matrix due to rapid reaction of Cl^- with hydroxyl radicals (•OH)[7].

Electrochemical treatment involving an electrocatalytic chlorine evolution reaction (CER)[8] at the anode is currently the preferred method to oxidize organic impurities[9]. Conventional electrochemical systems[10] use ultraviolet (UV) irradiation to dissociate the hypochlorous into reactive chlorine species and •OH (Fig. 1b). In the hypersaline backgrounds, the concentrations of Cl• and ClO• are comparable to or even higher than that of •OH[11]. Through either hydrogen abstraction or chlorination of unsaturated C–C bonds, reactive chlorine species transform organic compounds into the chlorinated intermediates. However, these intermediates are resistant to •OH oxidation and pose a greater hazard than their parent compounds[12], with well documented health risks, including the induction of bladder cancer and birth defects[13]. Their removal by conventional reactors has been proven to be costly in previous reports[14]. In conclusion, the effective and economical removal of organic contaminants from hypersaline wastewater remains a long-standing challenge.

Recently, we showed that by using the two photoelectrodes in a photoelectrochemical cell[15] the reduction of H_2O to atomic hydrogen (H*) on the cathode and OH^-/H_2O oxidation to •OH on the anode can occur concurrently to achieve redox-neutral electrochemistry[16]. Chlorinated organics, such as trichloroacetic acid and *p*-chloroaniline, were effectively mineralized in this system[17]. On the basis of these findings, we reasoned that if C–Cl bonds in chlorinated intermediates can be catalytically cleaved to generate the carbon-centred radicals on the cathode the radical–radical cross-coupling •OH addition reaction can continue along the chlorination–dehalogenation–hydroxylation (CDH) path (Fig. 1c). The CDH path will perfectly address the challenge of handling chlorinated intermediates generated during hypersaline wastewater treatment. Furthermore, •OH addition for mineralization of organic contaminants in the CDH route could be more effective when compared with the reported conversion path involving •OH addition, O_2• formation and HOO• abstraction, which requires dissolved O_2 for electrophilic reaction in conventional electrochemical advanced oxidation processes[18].

Current electrochemical cells (Fig. 1b) cannot achieve the proposed CDH reaction because the large gap between the anode and cathode prevents the radicals from reaching each other fast enough[19]. Further, using salt-containing water for electrolysis causes cations and protons to compete for charge transport across the cell. Poor mass transfer in the presence of Na^+ ions causes H^+ from the oxygen evolution reaction (OER) to remain near the anode, lowering the local pH and triggering a large pH gradient across a conventional electrochemical reactor[20]. This increases the thermodynamic potential of both anode

https://doi.org/10.1038/s41565-024-01669-3

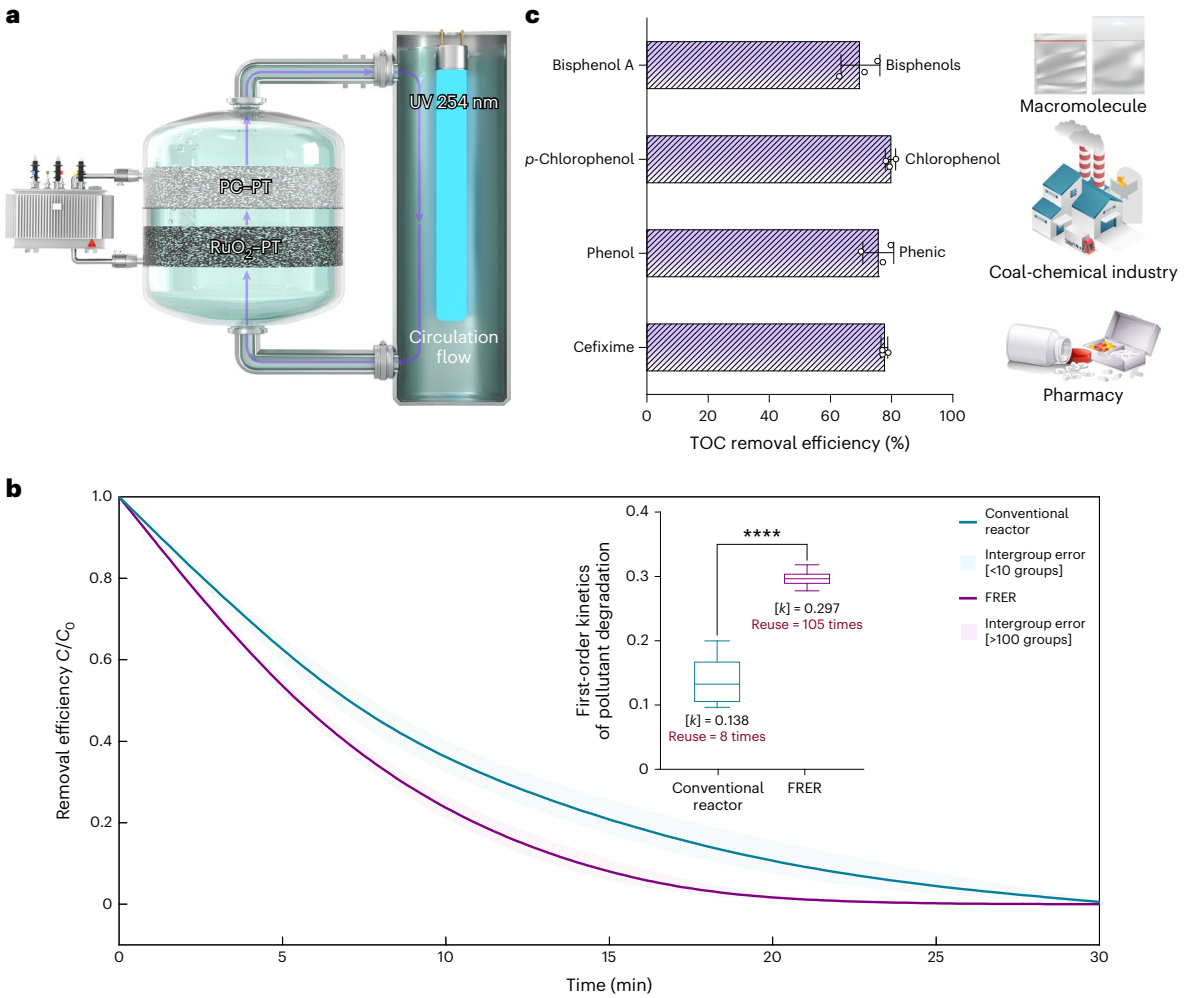

Fig. 2 | Bench-scale FRER effectively decomposes various organic compounds. a, Illustration of the FRER. The RuO_2–PT anode and PC–PT cathode are assembled ~4.0 mm apart in the electrochemical cell. Production of reactive chlorine in the electrochemical unit initiates the reaction. With chlorine pumping into the UV region, chloro-intermediates will be attacked by photolysed reactive species. **b**, Graph showing that the FRER degrades BA more effectively than a conventional reactor installed with the same types of electrode as FRER. The inset compares the degradation kinetics of both electrochemical reactors over 20 min. C/C_0 is the ratio of the concentration of organic matter at different time points to its initial concentration. Lines inside the box represent the average value, boxes represent the interquartile range and whiskers represent the minimum and maximum values. ****$P < 0.0001$. **c**, Mineralization efficiencies of typical chemical pollutants from different industries. The data are plotted as mean ± s.d. ($n = 3$). Reaction conditions: initial pollutant concentration 50 ppm; current density 20 mA cm^{-2}; electrolyte containing 0.5 M NaCl.

and cathode and raises the voltage in conventional reactors. Moreover, random dissipation of low-grade heat and limited Cl^- mass transfer also causes rapid electrochemical conversion of RuO_2 on the anode to volatile RuO_4. Such corrosion shortens the operation lifetime of the current RuO_2-based anode in electrochemical cells[21].

Here, we report the flow-through redox-neutral electrochemical reactor (FRER), which can effectively remove the organic impurities from hypersaline wastewater following the proposed CDH degradation pathway. Our reactor isolates the UV irradiation component from the electrochemical cell and achieves flow-through via water circulation. The anode and cathode, which are respectively RuO_2- and palladium cluster (PC)-coated porous titanium (PT), are installed just 4 mm apart. We show that continuous output of chlorine from the electrochemical cell initiates the oxidation of organic compounds. PCs on the cathode activate chlorinated intermediates to carbon-centred radicals, which are thermodynamically favourable for •OH radical coupling to form hydroxylated aromatic ring intermediates. CDH cycling mineralizes the organic impurities in hypersaline waters into CO_2 and H_2O. The FRER reactor has operated continuously for two months using real hypersaline wastewaters from a coal-fired power plant and coal-chemical enterprise. FRER-ED, an integration of ED with FRER, is 63.3% and 54.7% cheaper and emits 82.6% and 67.7% less CO_2 than the multi-effect evaporation-crystallization and mechanical vapour compression (MVC) evaporation-crystallization techniques, respectively, potentially forming the next generation of industrial reactors.

Construction and performance of bench-scale FRER

The UV irradiation component of our FRER is isolated from the electrochemical cell through water circulation (Fig. 2a). The electrodes in our reactor are just 4 mm apart (versus 2 cm in conventional reactors). We used RuO_2- and PC-coated PT as anode and cathode, respectively. To achieve superior CER at the anode, RuO_2 was thoroughly coated on the inside and outside surfaces of the PT by repeatedly painting with Ru-containing precursor and optimizing the annealing temperature under air conditions[22]. X-ray diffraction spectra of RuO_2-coated PT (RuO_2–PT) displayed diffraction peaks that are consistent with a solid solution of rutile RuO_2 (Supplementary Fig. 1a)[23]. Scanning electron microscopy–energy-dispersive X-ray spectroscopy (SEM-EDS) showing

https://doi.org/10.1038/s41565-024-01669-3

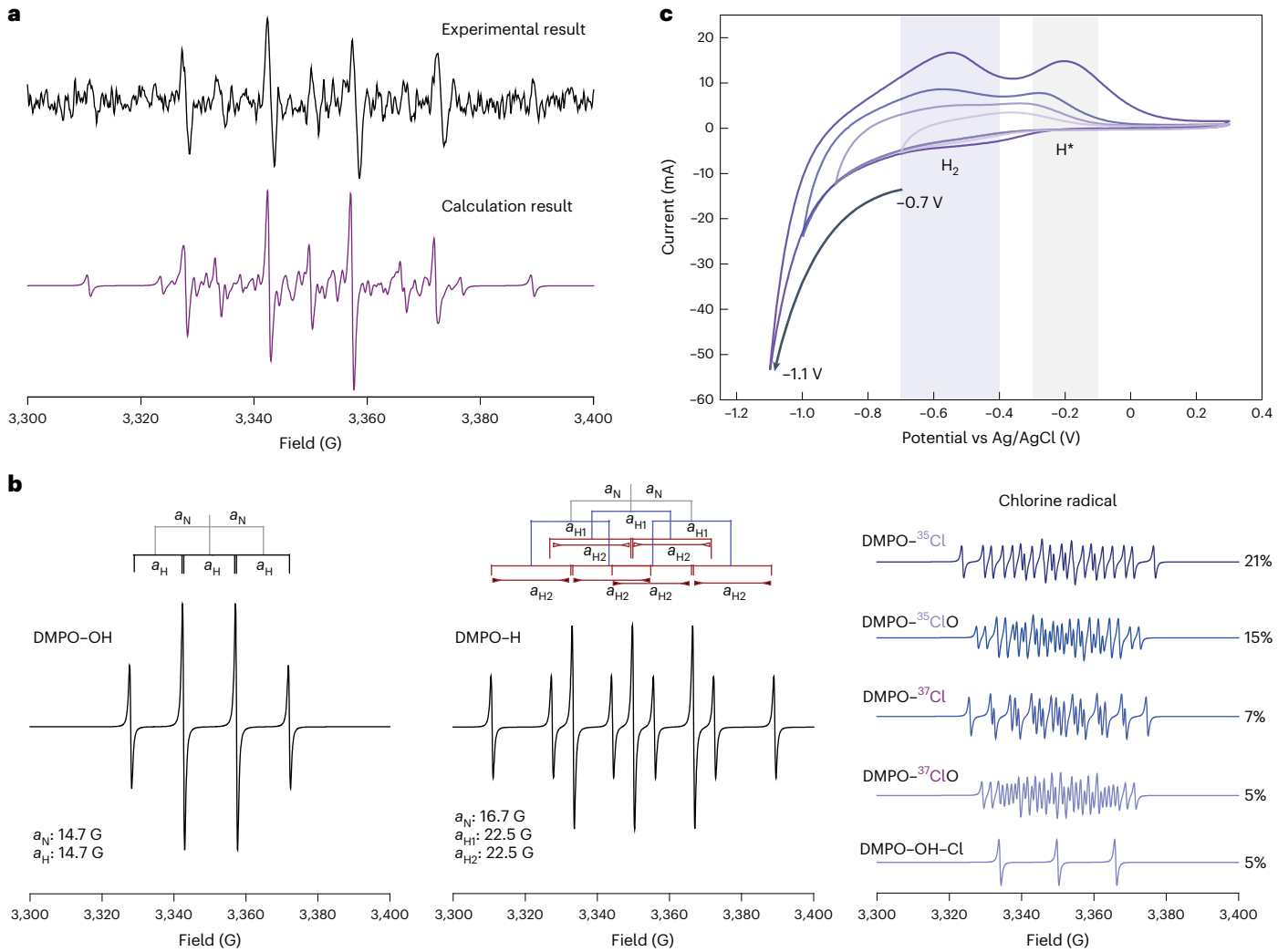

Fig. 3 | Identification and quantification of various radicals in FRER. **a**, Experimental (black) and calculated (purple) EPR spectrum of DMPO adducts recorded in FRER. Reaction conditions: current density, 20 mA cm^{-2}; DMPO concentration, 1.0 ppm; electrolyte containing 0.5 M NaCl. **b**, Quantitative analysis of EPR spectra from the FRER using density functional theory (DFT) calculation reveals signals that belong to •OH, •Cl and ClO• radicals and atomic H. **c**, Cyclic voltammetry of PC–PT in a 0.5 M NaCl solution. When starting potentials are from HER potential (−0.70 V versus Ag/AgCl), as-generated hydrogen species in the reduction stage are oxidized in the oxidation stage. Oxidation peaks between −0.7 and −0.4 and between −0.35 and 0 V versus Ag/AgCl correspond to oxidation of H_2 (purple shaded area) and H* (grey shaded area), respectively.

even dispersion of Ru elements in a TiO_2 matrix confirms successful deposition of the CER active layer (Supplementary Fig. 1b).

For Pd coating, we used magnetron sputtering (Supplementary Fig. 2a) because depositing nanosized Pd from Ar plasma will not damage the porous structures of PT[24] (Supplementary Fig. 2b). Cross-sectional images and EDS analysis show that the interconnected three-dimensional (3D) pores in PT enabled Pd ions to diffuse effectively into the electrode subsurface (Supplementary Fig. 2c). High-angle annular dark-field scanning transmission electron microscopy reveals uniformly distributed PCs on PT (Supplementary Fig. 2d)[25]. Deconvoluted surface-sensitive X-ray photoelectron spectroscopy spectra of Pd 3d revealed a peak at ~335.0 eV, which was ascribed to the metallic state of Pd^0 (Supplementary Fig. 2e). Only a small amount of $Pd^{\delta+}$ ($\delta < 2$) species was confirmed on the surface of the electrode. We deduced that the magnetron-sputtered Pd ions were strongly stabilized with PT substrate after annealing under N_2 conditions, resulting from the formation of Ti–Pd moieties[26].

To test the FRER, we used it to decompose benzoic acid (BA) from a highly saline (~2.5%) solution and compared its performance with a conventional reactor that uses the same types of electrode. At a current density of 20 mA cm^{-2}, the FRER, with an electrode area to solution volume ratio of 8×10^{-3}, achieved complete degradation of BA with an initial concentration of 50.0 mg l^{-1}. The rate constant was 2.2 times higher than that in the conventional reactor (Fig. 2b). The PT cathode coated with PC had the fastest transformation rate (0.31 min^{-1}), followed by those coated with Pd nanoparticles (0.20 min^{-1}), PdO nanoparticles (0.16 min^{-1}) and PT (0.13 min^{-1}) (Supplementary Fig. 3a–c). Within 40 min, the FRER with a PC-decorated PT (PC–PT) cathode achieved over 66.0% total organic carbon (TOC) removal. This surpasses the performance of both a conventional reactor (35.0%) and a FRER with a PT cathode (52.0%) (Supplementary Fig. 3d). More importantly, the FRER is significantly more stable than a conventional reactor. The s.d. of BA degradation rate for 105 continuous cycles in FRER was only 0.01 (inset in Fig. 2b).

We further used our FRER to remove bisphenol A, chlorophenol, phenol and cefixime, which are typical pollutants found in hypersaline landfill leachates and wastewaters from pharmaceutical and coal-to-chemical facilities (Fig. 2c). All organic compounds with an initial concentration of 100.0 mg l^{-1} in highly saline water (2.5%) were degraded for 2 h. Chlorophenol- or phenol-containing water achieved a

mineralization efficiency of nearly 80.0%. The TOC removal efficiencies in the refractory bisphenol A- and cefixime-containing highly saline waters were more than 70.0% and 78.0%, respectively.

Identification of redox radical pairs in FRER

To understand the effective mineralization performance of the FRER, we used electron paramagnetic resonance (EPR) analysis to study the compositions of the reactive species. The EPR spectrum from the FRER under flow mode is clearly different from that of the conventional reactor without flow (Supplementary Fig. 4). In addition to the 5,5-dimethyl-1-pyrroline-*N*-oxide (DMPO) adduct from the •OH radical, we observed other adducts in the FRER (Fig. 3a). Importantly, we successfully analysed the EPR spectra using Gaussian computations and confirmed that two signals in the photoexcited hypersaline solution belong to DMPO-^{35}Cl and DMPO-^{37}Cl while residual signals are from DMPO-^{35}ClO, DMPO-^{37}ClO and DMPO–OH(ClO) (Fig. 3b and Supplementary Fig. 5)[27]. The dominant signal with nine peaks is assigned to DMPO–H.

Further monitoring of reactive species produced at the electrodes revealed the co-existence of redox radical pairs. Testing the electrocatalytic oxidation of 0.5 M Cl^- in saline water with a RuO_2–PT anode and various PT cathodes, we found that Cl_2 and HOCl/OCl^- were produced at a constant rate of 0.03 mmol min^{-1} across all types of cathode (Supplementary Fig. 6). These results indicate that the separate UV irradiation in the FRER reliably photolyses the chlorine into reactive chlorine species (Cl• or ClO•) and •OH radicals.

Cyclic voltammetry and EPR experiments further confirmed the production of H* from the cathode. The weak ninth characteristic peak of DMPO–H in the EPR spectrum was assigned to the trapping of H* from PT (Supplementary Fig. 7a). When PC–PT was applied, the as-generated H* with starting potential from the hydrogen evolution reaction (HER) overpotential (less than −0.70 V versus Ag/AgCl) was clearly oxidized in the oxidation stage (Fig. 3c)[28]. The EPR peak intensity of DMPO–H was much stronger than when pristine PT was applied. The H* oxidized peak intensity was much higher using PC–PT than Pd–PT (Supplementary Fig. 8a). This implied that H_2O can be effectively dissociated into H* by PC–PT. We found that clustered Pd decreased the dissociation energy of H_2O to 0.99 eV, which is much lower than that with Pd(111) (2.06 eV) (Supplementary Fig. 8b). The Bader charge of Pd atoms on Pd(111) is 10.04, which is obviously lower than that on PCs (10.97). More valence electrons of PCs facilitate the charge transfer to H_2O, promoting stronger bonding interaction and orbital hybridization. This enables H_2O to reach the metastable state and accelerates its dissociation, so that the PC can cleave the O–H bond to produce H* and is resistant to H_2O poisoning[29].

We also investigated the effect of mass transport on the composition of reactive species in the FRER. Higher flow-through rates increased the intensity of DMPO–Cl and DMPO–OH EPR signals, indicating that the strongly oxidative chlorine intermediates can be obtained with higher flow velocity (Supplementary Fig. 9).

Redox-neutral mechanism for efficient TOC removal

Using different quenchers, we show that the radicals in this FRER had varying roles. Methanol, which quenches the •OH radicals both on the anode surface and in bulk solution[30], retarded BA transformation to the same extent as *t*-butanol, which quenches •OH radicals only in the bulk (Supplementary Fig. 10). This indicates that the primary pathway for electrochemical oxidation of BA is •OH radical-mediated oxidation in the bulk rather than an electrical double layer close to the anode surface.

H* also plays a key part in the degradation of organic compounds. Quenching H* through O_2 aeration significantly decreased TOC removal. High-resolution mass spectrometry (HRMS) further supports the extensive involvement of H* (Fig. 4a). Several chlorinated BAs, especially monochlorobenzoic acid and dichlorobenzoic acids, which were seen at the start, were depleted after 20 min in the FRER with PC–PT electrodes. In contrast, in the FRER with pristine PT electrodes, the chlorinated BA species persisted for up to 40 min (Fig. 4a and Supplementary Fig. 11).

On the basis of the calculated condensed Fukui function, which showed that the *para*-position of BA is most reactive (Supplementary Fig. 12), we studied the transformation of *p*-chlorobenzoic acid (PCBA) by cyclic voltammetry. Scans were primarily recorded with the glass carbon and Pt electrodes in 200:1 MeCN:H_2O (0.1 M tetrabutylammonium tetrafluoroborate, $TBABF_4$) electrolyte (Supplementary Fig. 13). An anodic sweep displaying a reversible redox wave (E1) at $E_{1/2}$ = −0.55 V versus Fc^+/Fc indicates the absorption of H atoms during the cathodic HER (Fig. 4b). The new cathodic wave (E2) at −1.0 V versus Fc^+/Fc and the corresponding anodic wave at 0.61 V that emerged on addition of PCBA signifies C–Cl bond cleavage by direct electron-transfer processes[31]. Moreover, the more prominent C–Cl bond cleavage wave at E2 on addition of H_2O indicates the H*-mediated dehalogenation via nucleophilic H addition or Cl abstraction[32].

Further, the change in the absorption spectra of PCBA shows a typical dehalogenation reaction (Fig. 4c). The weakening of the characteristic absorption intensity of PCBA during the electrochemical reaction and the appearance of a new shoulder peak at 225 nm that coincides with the characteristic absorption peak of BA indicates that PCBA underwent a dechlorination reaction at the Pd interface[33]. To trace the carbon-centred radicals involved in the electrochemical process, EPR spin trapping was used. Phenyl-*N*-*t*-butylnitrone (PBN) was employed as the spin trap agent because it is capable of forming environmentally persistent carbon-centred radical adducts[34]. Under anaerobic conditions, no obvious PBN spin adducts were observed (blue spectra in Fig. 4d). Using Pt as the counter-electrode, new PBN spin adducts that emerged upon addition of PCBA were assigned to trapped carbon-centred radicals (red spectra in Fig. 4d and Supplementary Fig. 14). When boron-doped diamond was used as the counter-electrode to produce •OH[35], HRMS confirmed the formation of hydroxybenzoic acid with high selectivity (Fig. 4e). These experiments unequivocally show that radical–radical cross-coupling occurred between the carbon-centred radicals and •OH (Supplementary Figs. 15 and 16). Because the hydroxylation is the key step in organic mineralization, the hydroxylation products are important intermediates.

We propose a scheme for the efficient decomposition of organic contaminants in hypersaline backgrounds (Fig. 4f). Depending on the nature of the chlorinated organic intermediates (R–Cl), protons can be transferred as H* or H^- for efficient dehalogenation on the Pd surface. R–Cl enables abstraction of an H atom from PdH^- or PdH_x to generate RH or R•[36]. Concurrently, the as-formed reductive Pd, being a good electron donor, ensures the formation of $RCl^{\bullet-}$, which fragments to form R•[37]. Electrons can also be injected into the unoccupied orbital of halogenated aromatics to give $R–Cl^{\bullet-}$. Subsequent intramolecular electron transfer from the π orbital to the antibonding σ^* orbital breaks the C–Cl bonds[38]. As a critical intermediate for two dechlorination paths, R• radicals are readily captured by a large amount of •OH in FRER. The synchronous CDH path in FRER is thermodynamically favourable for –OH addition to complete the ring-opening reaction and remove the organic contaminant.

Although HRMS shows that mono- and dichlorinated BA diminished rapidly in the FRER with PC–PT, the intensity of dichlorohydroxybenzoic acids is higher in this system than in the FRER with pristine PT (Supplementary Fig. 17). Dichlorohydroxybenzoic acids are formed via hydroxylation and rechlorination (Supplementary Fig. 18). Further cycles of CDH produce dihydroxybenzoic acid (Supplementary Fig. 19), followed by ring opening to form low-molecular-weight organic acids before mineralization[37]. Such acids, which were observed experimentally (Supplementary Fig. 20), would decompose into CO_2 and Cl^- after CDH cycling.

https://doi.org/10.1038/s41565-024-01669-3

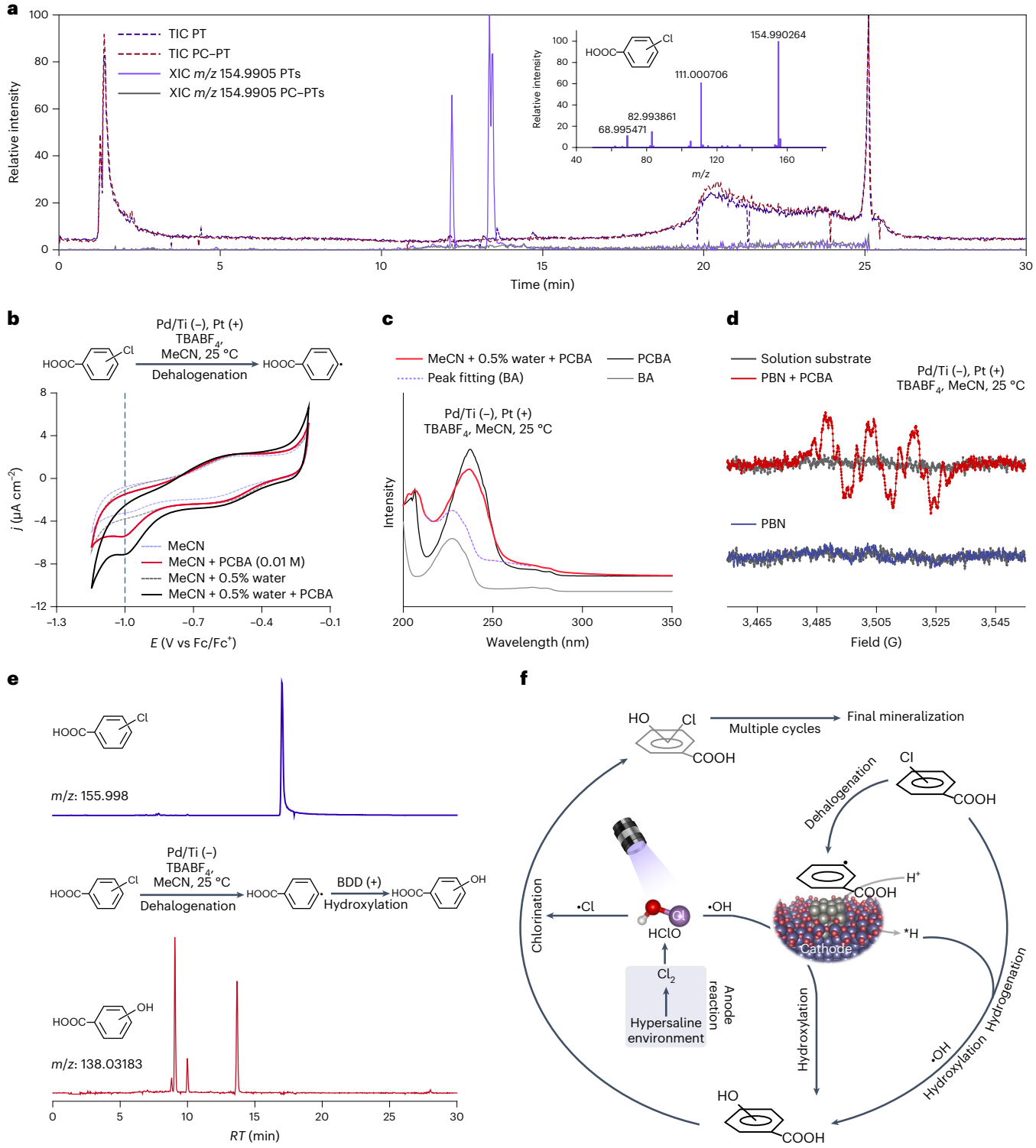

Fig. 4 | Radical–radical cross-coupling removes TOC in FRER. a, Total ion chromatogram (TIC) of BA degradation products and extracted ion chromatogram (XIC) of PCBA produced when using PC–PT and pristine PT electrodes in the FRER. Inset: secondary mass spectrum of chlorinated BA. **b**, Chemical equation for dechlorination of PCBA into carbon-centred radicals (top), and cyclic voltammetry scans of PC–PT in MeCN and 200:1 MeCN:H_2O (0.1 M $TBABF_4$) electrolyte with and without PCBA (bottom). Blue dashed line, reduction potential of PCBA. The intensified Pd–H peak is derived from H_2O. **c**, UV–vis spectra showing electrochemical transformation of PCBA in MeCN electrolyte. Grey line, BA reference. The new absorbance peak at 235 nm after 10 min corresponds to BA (purple dashed line). **d**, EPR spectrum of PBN adducts recorded in FRER. Backgrounds are solutions without PCBA or PBN (black) and with only PBN (blue). **e**, XIC of PCBA (top) and hydroxylated product (bottom) in FRER with PC–PT and boron-doped diamond (BDD) electrodes as working electrode and counter-electrode, respectively. The electrochemical equation for the hydroxylation of carbon-centred radicals to hydroxybenzoic acid is shown in the middle. **f**, Proposed radical–radical cross-coupling mechanism for TOC removal from hypersaline solutions in FRER. Key steps are (1) chlorination of organic substrate, (2) dehalogenation of chlorinated by-products and (3) hydroxylation of as-produced carbon-centred radicals. Cycling through this process effectively removes organic compounds.

https://doi.org/10.1038/s41565-024-01669-3

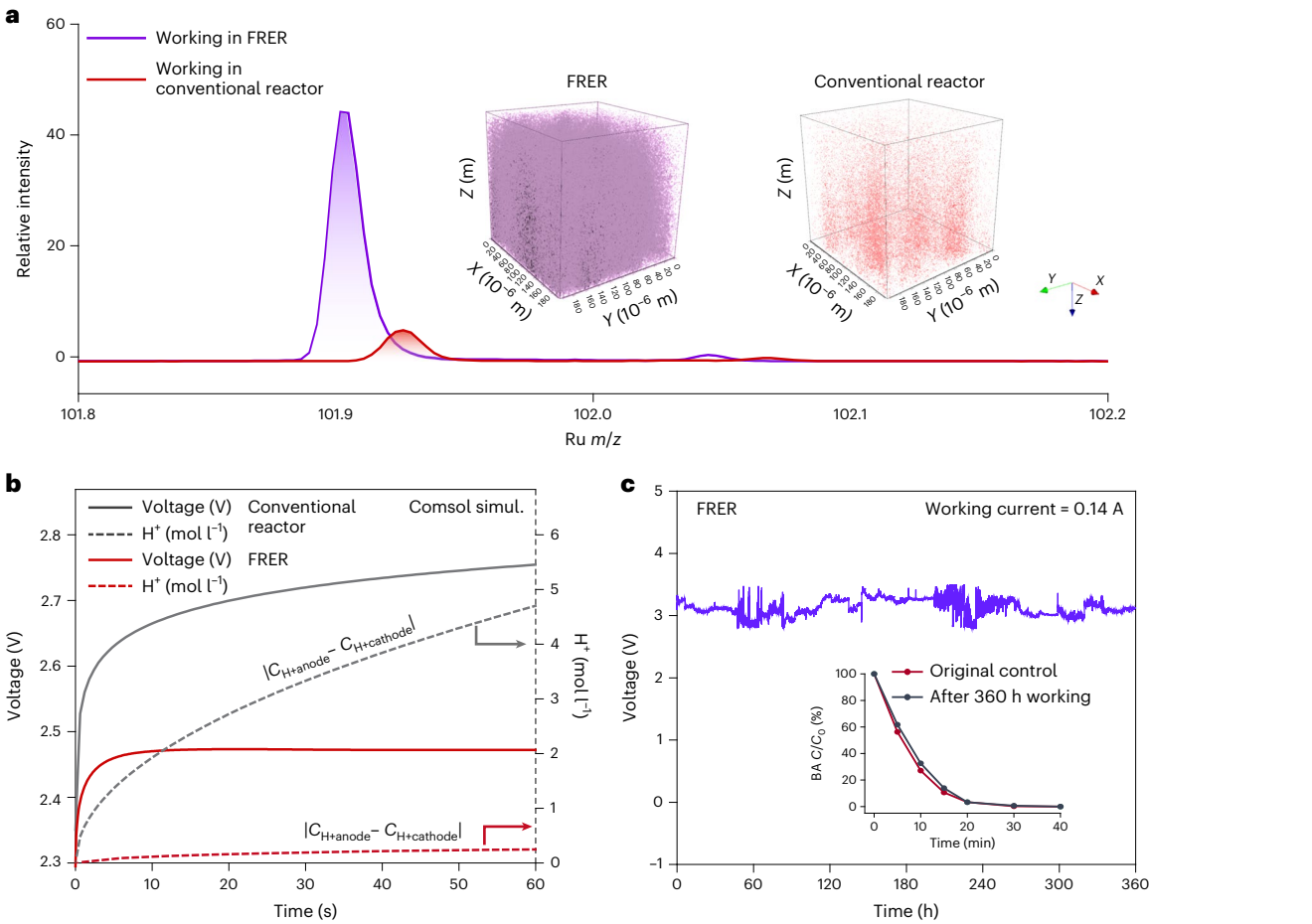

Fig. 5 | The FRER is sufficiently stable for extended operation. a, Mass spectrum of TOF-SIMS depth profiling of RuO_2–PT anode after being used in the FRER for 360 h (purple) and a conventional reactor for 24 h (red). Inset: 3D TOF-SIMS tomography of Ru distribution in the used RuO_2–PT. **b**, Simulated cell voltage (left axis) and H^+ concentration difference between electrodes (right axis) in the FRER (red curves) and a conventional reactor (grey curves). **c**, Cell voltage data show that the FRER operates stably for 360 h in a high-saline background. Inset: the FRER degraded BA with the same efficiency as the original control even after operating for 360 h.

Practical applications of FRER

Corrosion is a key problem in many electrochemical systems. Active sites on Ti substrates used for chlorine production are known to be stripped of Ru^{IV} to form volatile RuO_4. Accordingly, we investigated the detachment of RuO_2 from the RuO_2–PT anode in both the FRER and a conventional reactor. Because surface oxides must form in the presence of OER[39], we assumed that the formation of volatile RuO_4 occurs through an intermediate that is accompanied by OER and that the rate of OER is a measure of the percentage of Ru released into the solution.

The low chlorine production efficiency observed in a conventional reactor suggests high Ru^{IV} corrosion at the RuO_2–PT anode (Supplementary Fig. 21). Indeed, time of flight secondary-ion mass spectrometry (TOF-SIMS) detected Ru after 24 h of operation (Fig. 5a) and visible amounts of detached RuO_2 layers were found after 48 h (Supplementary Fig. 22a). When compared with 3D TOF-SIMS tomography of an unused RuO_2–PT that showed a vertical gradient distribution of Ru and Ti (Supplementary Fig. 22b), almost no Ru signals were detected from the anode after operating for 24 h in a conventional reactor (right inset in Fig. 5a).

In contrast, the RuO_2 coating in the FRER remained stable for up to 360 h (Fig. 5a). 3D TOF-SIMS tomography shows that both the Ru signal and the distinct boundary between the RuO_2 layer and Ti substrate in RuO_2–PT were largely unchanged after 360 h (left inset in Fig. 5a and Supplementary Fig. 22c). This stability indicates high selectivity for CER over OER at the anode in the FRER. Enhanced mass transport in the FRER, which supplies sufficient Cl^- ions near the anode for CER, reduces the likelihood of OER, which drives the formation of volatile RuO_4 (Supplementary Fig. 23)[40].

Further, rapid consumption of H^+ during chlorine production primarily reduced the intrusion of H^+ from anode to cathode (Fig. 5b). To balance the electrical charge due to electron flux, Na^+ migrates from the anode to the cathode, and OH^- produced by HER that is not neutralized by protons increases catholyte pH. This could form large pH differences that will increase the thermodynamic potential for the whole reaction and decrease the overall energy efficiency. In the conventional reactor we examined, the cell voltage for sustaining a current density of 1.0 mA cm^{-2} increased by 60.0% after only 10 min of operation, while the increase was <5.0% in the FRER (Supplementary Fig. 24). The fluctuations seen in Fig. 5c are due to periodic evolution of H_2 gas bubbles from the surface and micropores of the porous structure that segregates the catalytic active sites from the electrolyte. Negligible voltage loss and the high BA degradation stability in the FRER over 360 h demonstrate that it is suitable for operating in highly saline brine.

We used the FRER to decontaminate actual samples of hypersaline wastewaters (Supplementary Table 1) from a thermoelectric power plant, a coal-chemical enterprise and a textile printing and dyeing plant in an on-site field experiment (Fig. 6a and Supplementary Fig. 25). The wastewater was presoftened with $Ca(OH)_2$ and Na_2CO_3. With a treatment cost of ~US$1.0 m^{-3}, less than 30% and 40% TOC can be removed using Fenton and ozone oxidation, respectively (Supplementary

https://doi.org/10.1038/s41565-024-01669-3

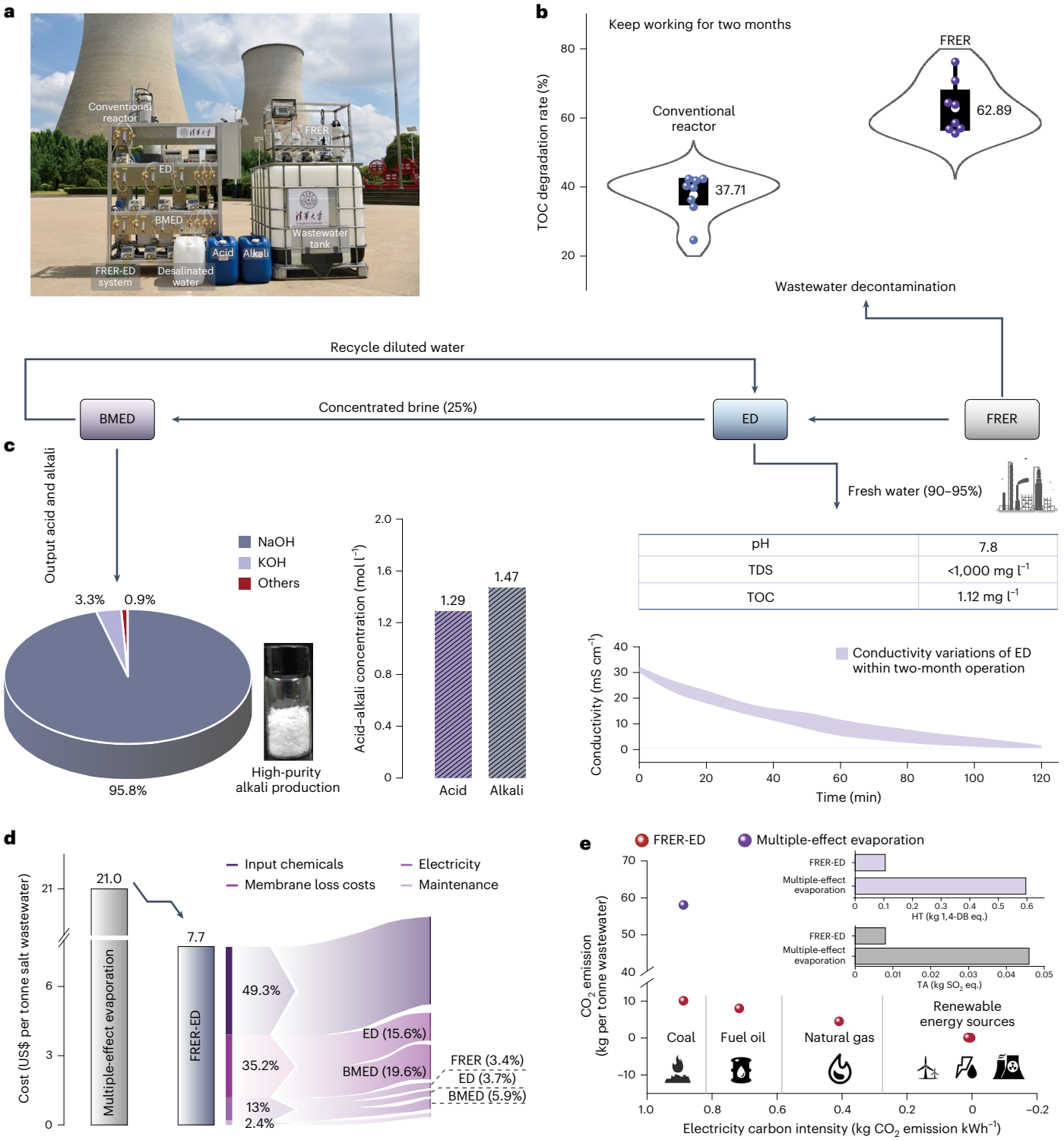

Fig. 6 | Field application of FRER-ED. a, Photograph showing experimental set-up for a FRER-ED experiment at a coal-fired power plant in Anhui, China. **b**, The TOC removal efficiency of the FRER is nearly twice as high as that of a conventional reactor. The average efficiency of the FRER remained at 62.89% after continuously decontaminating real desulfurized wastewater for 2 months. The solid circle is the TOC removal efficiency from 1 week of operation, with width in the density plot reflecting data frequency and height representing the 95% confidence interval. White dots within the strip frames signify the mean, and black frames denote the interquartile range. **c**, Recovery of clean water, purified NaOH and acid from FRER, ED and BMED. Inset table: water quality of desalinated water from ED. The purple shaded area in the graph shows the change in conductivity of ED over two months of operation. The purity of liquid alkali (pie chart), as-produced NaOH (photo) and concentrations of liquid alkali and acid (histogram) from BMED are shown. **d**, Treating each cubic metre of desulfurized wastewater with FRER-ED costs less than with current multiple-effect methods. The cost for FRER-ED includes chemicals, membrane replacement, electricity and maintenance. **e**, CO_2 emission for current multiple-effect method (purple circle) and FRER-ED (red circles) using electricity from different sources. Inset: histograms comparing the impacts of the two systems on HT and TA.

Fig. 26). On the basis of bench-scale experiments, we applied a voltage of 3.5 V for field electrochemical treatment (Supplementary Fig. 27). At an electrode area to solution volume ratio of 0.01, the FRER can remove almost 80% TOC from the desulfurized wastewater (Supplementary Fig. 28). This is nearly 2.0 times higher than when using the conventional reactor (Fig. 6b). After two months of continuous operation, the current density of the FRER remained at 20.0 mA cm^{-2} with a TOC removal efficiency of >62.5% (Fig. 6b and Supplementary Fig. 29). With an increase in current density to 40 mA cm^{-2}, the TOC removal efficiency was improved by 10% (Supplementary Fig. 30). The FRER could also remove 65% and 70% TOC within 2 h from reverse osmosis concentrated wastewater from a coal-chemical plant, and hypersaline wastewater from a textile printing and dyeing plant, respectively (Supplementary Fig. 31).

Following FRER decontamination, ED isolates the salt from as-purified water[41]. Our system showed a NaCl removal ratio of 98.0% and current efficiency of 89.6% (Supplementary Table 2). Up to 95% desalinated clean water was recovered using this system (table in Fig. 6c). We evaluated the toxicity of as-produced water by examining its effects on zebrafish survival, morphology and heart rate[42]. The water from PT-based FRER, which contained chlorinated intermediates, caused 25% death and a malformation rate of 15.0% at 96 h (Supplementary Fig. 32a–c). Both death and malformation rate decreased, to 15.0% and 8.0% respectively, when water from PC–PT-based FRER was used. More importantly, the effective removal of pollutants allowed the ionic mobility of the ED system to remain at nearly the same level over two months of continuous use (Fig. 6c). After periodic chemical cleaning, neither extracellular polymeric substances nor live/dead cells were observed on the membrane using a confocal laser scanning microscope (Supplementary Fig. 33). SEM images show that both the anion- (AEM) and cation-exchange (CEM) membranes exhibit dense and homogeneous matrices without depositions, holes or cracks (Supplementary Fig. 34). This is in sharp contrast to the severe membrane fouling and obvious ionic mobility decrease when treating wastewater with inferior TOC removal (Supplementary Fig. 35). The FRER also has the potential to remove organics from concentrated brine (total dissolved solids ~9%) after ED (Supplementary Fig. 36). Dissolved salts in the decontaminated hypersaline wastewaters were sustainably converted into NaOH (1.5 M, purity > 95%) and acid (1.3 M) using BMED (Fig. 6c and Supplementary Fig. 37). Moreover, after the two-stage ED process, the feed with total dissolved solids of ~18% enabled an increase in the concentration of NaOH and acid to 3.0 M (Supplementary Fig. 38). After vaporization, we obtained pure alkali, ascribed to the superior TOC removal performance of the FRER-ED process. When using a conventional reactor with ED, the product has a light-yellow colour due to the presence of residual organic impurities in the background (Supplementary Fig. 39).

FRER-ED is economical and has a low environmental footprint

We compared the capital expenditure of our system with current salt crystallization technologies (Supplementary Table 3)[43]. Herein, FRER-ED cost calculation included chemical reagents (49.3%) and electricity (13.0%), as well as amortization (37.6%). With the conventional reactor and advanced oxidation process that suffer from obvious membrane fouling, the cost for the membranes (35.2%) would increase markedly (Supplementary Table 4). Considering these factors, our estimates show that operation cost for FRER-ED is 63.3% lower than for the multi-effect evaporation-crystallization technologies (Fig. 6d) and 56.7% lower than the evaporation-crystallization process using MVC technology.

Deploying ion migration for production of water, alkali and acid means shifting from multi-effect evaporation crystallization to an electrically driven resource recovery. To contextualize this shift, we performed and compared the life-cycle assessment (LCA) for FRER-ED and for multi-effect evaporation-crystallization systems that use high-temperature steam and produce hazardous solid waste salts. For generic salt crystallization using the multi-effect evaporator, the global warming potential (GWP), terrestrial acidification (TA) and human toxicity (HT) were estimated to be of the order of 58.0 kg of CO_2 equivalent, 4.6×10^{-2} kg of SO_2 equivalent and 0.6 kg of 1,4-dichlorobenzene (1,4-DB) equivalent, respectively. When applying MVC as the evaporation technique, GWP decreased to 31.3 kg of CO_2 equivalent, while TA slightly increased to 5.4×10^{-2} kg of SO_2 equivalent.

With FRER-ED, nearly all the environmental impacts were significantly reduced (Supplementary Table 5). CO_2 emission dropped to 10.1 kg even when electricity from a traditional thermal power plant was used (Fig. 6e). TA and HT also decreased to 8.1×10^{-3} kg of SO_2 equivalent and 0.1 kg of 1,4-DB equivalent, respectively. When green electricity with carbon intensity of less than 12 g of CO_2 equivalent per kilowatt-hour from hydro, wind or nuclear is used, FRER-ED on average decreased GWP by more than 99.0%, HT by 97.0% and TA by 99.0% when compared with multi-effect or MVC evaporation crystallization (inset in Fig. 6e and Supplementary Table 6).

According to our estimates, deploying FRER-ED to treat the 1,500 million cubic metres of hypersaline wastewater released annually in China could potentially result in savings exceeding US$17 billion and a reduction of 52 million tonnes of CO_2 emissions. 1,400 million cubic metres of water and 16 million tonnes of alkali could be recovered (Supplementary Table 7). Such a sustainable recovery of resources could offset subsequent industrial production activities, which is in line with initiatives in advanced circular economy[44] and the global sustainable development goals[45].

Conclusions

Current technologies for recovering resources from hypersaline wastewaters are ineffective, expensive and energy intensive. They produce impure products and hazardous by-products, and suffer from membrane fouling. We solve these issues by developing an integrated FRER-ED system. Unlike conventional reactors running advanced oxidation processes, the FRER, which incorporates a thermodynamically electrochemical favourable CDH mineralization path, had potential to remove organic impurities from different hypersaline wastewaters. With excellent decontamination capabilities, the FRER reduced the membrane fouling and thereby operation cost of the subsequent ED used for desalination and recovery of clean water, and high-purity alkali and acids. When compared with the current multi-effect evaporation-crystallization technique, FRER-ED reduced operation cost by 63.3% and CO_2 emissions by 82.6%. The desalinated water, NaOH and acid obtained from our system has potential to offset industrial production activities. This accelerates the shift towards more efficient, electrically driven 'zero-discharge' technology, moving away from energy-intensive steam-driven processes. In the future, the implementation of optimized automation systems and industrial-scale PC–PT electrodes will be essential for manufacturing standard skid-mounted electrochemical devices suitable for practical applications.

Online content

Any methods, additional references, Nature Portfolio reporting summaries, source data, extended data, supplementary information, acknowledgements, peer review information; details of author contributions and competing interests; and statements of data and code availability are available at https://doi.org/10.1038/s41565-024-01669-3.

References

1. Chung, M. G., Frank, K. A., Pokhrel, Y., Dietz, T. & Liu, J. Natural infrastructure in sustaining global urban freshwater ecosystem services. *Nat. Sustain.* **4**, 1068–1075 (2021).
2. Zhang, X. et al. Managing nitrogen for sustainable development. *Nature* **528**, 51–59 (2015).

3. Panagopoulos, A. & Giannika, V. Comparative techno-economic and environmental analysis of minimal liquid discharge (MLD) and zero liquid discharge (ZLD) desalination systems for seawater brine treatment and valorization. *Sustain. Energy Technol. Assess.* **53**, 102477 (2022).
4. Menon, A. K., Haechler, I., Kaur, S., Lubner, S. & Prasher, R. S. Enhanced solar evaporation using a photo-thermal umbrella for wastewater management. *Nat. Sustain.* **3**, 144–151 (2020).
5. Kumar, A., Phillips, K. R., Thiel, G. P., Schröder, U. & Lienhard, J. H. Direct electrosynthesis of sodium hydroxide and hydrochloric acid from brine streams. *Nat. Catal.* **2**, 106–113 (2019).
6. Shehzad, M. A. et al. Shielded goethite catalyst that enables fast water dissociation in bipolar membranes. *Nat. Commun.* **12**, 9 (2021).
7. Zhang, W. et al. Impact of chloride ions on UV/H_2O_2 and UV/persulfate advanced oxidation processes. *Environ. Sci. Technol.* **52**, 7380–7389 (2018).
8. Chen, Y. et al. Tip-intensified interfacial microenvironment reconstruction promotes an electrocatalytic chlorine evolution reaction. *ACS Catal.* **12**, 14376–14386 (2022).
9. Liu, J., Zhang, X. & Li, Y. Photoconversion of chlorinated saline wastewater DBPs in receiving seawater is overall a detoxification process. *Environ. Sci. Technol.* **51**, 58–67 (2017).
10. Yang, T. et al. Efficient degradation of organoarsenic by UV/chlorine treatment: kinetics, mechanism, enhanced arsenic removal, and cytotoxicity. *Environ. Sci. Technol.* **55**, 2037–2047 (2021).
11. Rao, U. et al. Structural dependence of reductive defluorination of linear PFAS compounds in a UV/electrochemical system. *Environ. Sci. Technol.* **54**, 10668–10677 (2020).
12. Guo, K., Wu, Z., Chen, C. & Fang, J. UV/chlorine process: an efficient advanced oxidation process with multiple radicals and functions in water treatment. *Acc. Chem. Res.* **55**, 286–297 (2022).
13. Choi, C. et al. Efficient electrocatalytic valorization of chlorinated organic water pollutant to ethylene. *Nat. Nanotechnol.* **18**, 160–167 (2023).
14. Fang, J., Fu, Y. & Shang, C. The roles of reactive species in micropollutant degradation in the UV/free chlorine system. *Environ. Sci. Technol.* **48**, 1859–1868 (2014).
15. Zhang, J., Zhang, G., Lan, H., Qu, J. & Liu, H. Synergetic hydroxyl radical oxidation with atomic hydrogen reduction lowers the organochlorine conversion barrier and potentiates effective contaminant mineralization. *Environ. Sci. Technol.* **55**, 3296–3304 (2021).
16. Llorente, M. J., Nguyen, B. H., Kubiak, C. P. & Moeller, K. D. Paired electrolysis in the simultaneous production of synthetic intermediates and substrates. *J. Am. Chem. Soc.* **138**, 15110–15113 (2016).
17. Min, Y. et al. Mimicking reductive dehalogenases for efficient electrocatalytic water dechlorination. *Nat. Commun.* **14**, 5134 (2023).
18. Dwinandha, D., Zhang, B. & Fujii, M. Prediction of reaction mechanism for OH radical-mediated phenol oxidation using quantum chemical calculation. *Chemosphere* **291**, 132763 (2022).
19. Atobe, M., Tateno, H. & Matsumura, Y. Applications of flow microreactors in electrosynthetic processes. *Chem. Rev.* **118**, 4541–4572 (2018).
20. Finke, C. E. et al. Enhancing the activity of oxygen-evolution and chlorine-evolution electro-catalysts by atomic layer deposition of TiO_2. *Energy Environ. Sci.* **12**, 358–365 (2019).
21. Karlsson, R. K. B. & Cornell, A. Selectivity between oxygen and chlorine evolution in the chlor-alkali and chlorate processes. *Chem. Rev.* **116**, 2982–3028 (2016).
22. Näslund, L.-Å. et al. The role of TiO_2 doping on RuO_2-coated electrodes for the water oxidation reaction. *J. Phys. Chem. C* **117**, 6126–6135 (2013).
23. Jiao, Y., Jiang, H. & Chen, F. RuO_2/TiO_2/Pt ternary photocatalysts with epitaxial heterojunction and their application in CO oxidation. *ACS Catal.* **4**, 2249–2257 (2014).
24. Morales-Guio, C. G. et al. Solar hydrogen production by amorphous silicon photocathodes coated with a magnetron sputter deposited Mo_2C catalyst. *J. Am. Chem. Soc.* **137**, 7035–7038 (2015).
25. Dong, C. et al. Fully exposed palladium cluster catalysts enable hydrogen production from nitrogen heterocycles. *Nat. Catal.* **5**, 485–493 (2022).
26. Xiong, H. et al. Engineering catalyst supports to stabilize PdO_x two-dimensional rafts for water-tolerant methane oxidation. *Nat. Catal.* **4**, 830–839 (2021).
27. Ghassemzadeh, L., Peckham, T. J., Weissbach, T., Luo, X. & Holdcroft, S. Selective formation of hydrogen and hydroxyl radicals by electron beam irradiation and their reactivity with perfluorosulfonated acid ionomer. *J. Am. Chem. Soc.* **135**, 15923–15932 (2013).
28. Xu, B., Chen, Z., Zhang, G. & Wang, Y. On-demand atomic hydrogen provision by exposing electron-rich cobalt sites in an open-framework structure toward superior electrocatalytic nitrate conversion to dinitrogen. *Environ. Sci. Technol.* **56**, 614–623 (2022).
29. Wang, J. et al. Ambient ammonia synthesis via palladium-catalyzed electrohydrogenation of dinitrogen at low overpotential. *Nat. Commun.* **9**, 1795 (2018).
30. Kakade, B. A., Tamaki, T., Ohashi, H. & Yamaguchi, T. Highly active bimetallic PdPt and CoPt nanocrystals for methanol electro-oxidation. *J. Phys. Chem. C* **116**, 7464–7470 (2012).
31. Zuo, K. et al. Electrified water treatment: fundamentals and roles of electrode materials. *Nat. Rev. Mater.* **8**, 472–490 (2023).
32. Wang, H.-X., Toh, W. L., Tang, B. Y. & Surendranath, Y. Metal surfaces catalyse polarization-dependent hydride transfer from H_2. *Nat. Catal.* **6**, 351–362 (2023).
33. Sakamoto, H. et al. Photocatalytic dehalogenation of aromatic halides on Ta_2O_5-supported Pt–Pd bimetallic alloy nanoparticles activated by visible light. *ACS Catal.* **7**, 5194–5201 (2017).
34. Walter, T. H. et al. Spin trapping in heterogeneous electron transfer processes. *Can. J. Chem.* **60**, 1621–1636 (1982).
35. Barroso-Martínez, J. S. et al. Real-time detection of hydroxyl radical generated at operating electrodes via redox-active adduct formation using scanning electrochemical microscopy. *J. Am. Chem. Soc.* **144**, 18896–18907 (2022).
36. Hong, J. et al. Metastable hexagonal close-packed palladium hydride in liquid cell TEM. *Nature* **603**, 631–636 (2022).
37. Van Buren, J., Prasse, C., Marron, E. L., Skeel, B. & Sedlak, D. L. Ring-cleavage products produced during the initial phase of oxidative treatment of alkyl-substituted aromatic compounds. *Environ. Sci. Technol.* **54**, 8352–8361 (2020).
38. Wang, Y., Wei, Y., Song, W., Chen, C. & Zhao, J. Photocatalytic hydrodehalogenation for the removal of halogenated aromatic contaminants. *ChemCatChem* **11**, 258–268 (2019).
39. Yang, J. et al. CO_2-mediated organocatalytic chlorine evolution under industrial conditions. *Nature* **617**, 519–523 (2023).
40. Over, H. Surface chemistry of ruthenium dioxide in heterogeneous catalysis and electrocatalysis: from fundamental to applied research. *Chem. Rev.* **112**, 3356–3426 (2012).
41. Lin, J. et al. Shielding effect enables fast ion transfer through nanoporous membrane for highly energy-efficient electrodialysis. *Nat. Water* **1**, 725–735 (2023).
42. Butler, J. D., Parkerton, T. F., Redman, A. D., Letinski, D. J. & Cooper, K. R. Assessing aromatic-hydrocarbon toxicity to fish early life stages using passive-dosing methods and target-lipid and chemical-activity models. *Environ. Sci. Technol.* **50**, 8305–8315 (2016).
43. Stinn, C. & Allanore, A. Selective sulfidation of metal compounds. *Nature* **602**, 78–83 (2022).

44. Zabaniotou, A. Redesigning a bioenergy sector in EU in the transition to circular waste-based bioeconomy—a multidisciplinary review. *J. Clean. Prod.* **177**, 197–206 (2018).
45. Andrew, R. M. Global CO_2 emissions from cement production. *Earth Syst. Sci. Data* **10**, 195–217 (2018).

Methods

Chemicals

BA (99% purity), sodium chloride, sodium sulfate, ammonium acetate, methanol (high-performance liquid chromatography grade, 99.90% purity), acetone, anhydrous ethanol, nitric acid and hydrofluoric acid were all purchased from Sinopharm Holding Beijing Chemical Reagent Co. (China). DMPO (97% purity) was purchased from Aladdin. All purchased reagents were used as received without further purification.

Preparation of porous electrodes

The preparation of porous substrates from Ti has been described in the literature previously. We adapted this approach and prepared the Ti porous electrode using a mixture containing Ti particles and polymer. The polymer was decomposed and Ti particles sintered together by thermal treatment, resulting in a porous structure with diameter 30 mm. Before use, the Ti foam was chemically polished with a mixture of hydrofluoric acid and nitric acid for 0.5 min to remove the oxide surface. A RuO_2 active layer was thoroughly coated on the internal and external faces of the Ti substrate, with the fabrication process involving repeatedly painting Ru-containing precursor and optimizing the annealing temperature under air conditions.

The magnetron sputtering approach was employed here as a tool to decorate the Pd film, in which nanosized Pd from Ar plasma has the potential to deposit onto substrate without damage pristine structures. To prepare the PC–PT, a pure Pd sputtering target (99.9%) was used to deposit nanosized Pd. The Pd nanoparticles were prepared by a cluster source based on direct current magnetron plasma sputtering and gas aggregation. Charged nanoparticles with different sizes were extracted and focused using electrostatic lenses. The electrodes were annealed in a N_2 atmosphere at 400 °C for 2 h. PC–PT was finally obtained through sonicating the as-prepared electrode to preserve Pd nanoparticles with size range less than 2.0 nm. The costs for the PC–PT and RuO_2–PT electrodes are listed in Supplementary Table 8.

Characterizations

The morphology of the electrode was observed using a high-resolution Zeiss field emission scanning electron microscope (GEMINISEM 500) coupled with EDS. Transmission electron microscope images and EDS were obtained using a high-resolution field emission scanning electron microscope (Hitachi S-5500). The crystal structure of the electrode was analysed using a Max 2500 X-ray diffractometer under the operating conditions of 40 kV and 40 mA with Cu Kα radiation. X-ray photoelectron spectroscopy was used to analyse the oxygen vacancy changes on the surface of the electrode using a 250XI Al Kα source spectrometer. Free radicals in aqueous solution were recorded on an EPR spectrometer (Bruker) with DMPO as spin-trapper agent. To record the carbon-centred radicals, PBN was used as spin-trapper agent. TOF-SIMS (TOF-SIMS 5-100, ION-TOF) investigated detachment of active sites from anodes. A special transfer vessel, which can directly transfer a sample from a glovebox to the vacuum chamber of the TOF-SIMS, was used to transfer the sample without it being exposed to the ambient air. The primary ion beam was a Bi_3^{++} beam (30 keV), with an incident angle of 45° and scan area of 200 μm × 200 μm. The sputter ion beam was an O_2^+ beam (1 keV), with sputter velocity of 0.316 nm s^{-1} for SiO_2.

Bench-scale FRER experiments

We engineered a FRER, in which the UV irradiation region (254 nm UV lamp) was isolated from the cell through a water-circulating mode. PC–PT and RuO_2–PT electrodes were assembled in the reactor with separation 4.0 mm. A mixed solution (168 ml) containing 500 mM NaCl and 50 ppm BA circulated in the reactor, with the current density set at 20 mA cm^{-2}. Bisphenol A, nitrophenol and phenol with initial concentrations of 50 ppm were selected as typical pollutants, which can be detected in high-salinity wastewater from landfill leachate, pharmaceutical and coal-to-chemical facilities. For comparison, the conventional reactor was composed of PC–PT and RuO_2–PT electrodes, with a separation of 2.0 cm; a 254 nm UV lamp was set between these two electrodes. The concentrations were measured using high-performance liquid chromatography (Waters Alliance e2698) equipped with a C18 column. The intermediates were analysed using a QE Orbitrap ultrahigh-resolution liquid chromatography mass spectrometry system (UHPLC-Q-Orbitrap). The TOC was measured using a TOC analyser (Shimadzu).

Electrochemical measurements

All electrochemical experiments were performed at ambient temperature using an Autolab potentiostat (PGSTAT302N, Metrohm), and were conducted using a three-electrode set-up. All aqueous measurements used an Ag/AgCl reference electrode. Non-aqueous measurements used a non-aqueous Ag/Ag^+ reference electrode as a pseudo-reference and were performed in dry and de-aerated solvents. All non-aqueous potentials were referenced to the $Fc^{+/0}$ redox couple. All glassware used for electrochemical measurements was soaked in aqua regia and thoroughly washed with Milli-Q water before use. The glassware was subsequently dried in an oven and then cooled while a stream of nitrogen was passed through the cell.

Cyclic voltammograms under various systems were measured with an Autolab potentiostat controlled with NOVA software. The working electrodes were the planar Pd/Ti, glass carbon and Pt, which were precleaned with CH_3CN and dried. A Pt mesh was applied as the counter-electrode. All cyclic voltammetry tests were performed in a CH_3CN–water mixture with 0.1 M $TBABF_4$ (Macklin, electrochemical grade) and purged with solvent-saturated N_2 to remove atmospheric O_2.

Electrochemical dechlorination was carried out in the CH_3CN–water mixture at a current density of 1.0 mA cm^{-2}. After 10 min reaction, the samples were evaluated using a Hitachi UV–Vis spectrophotometer. The hydroxylation reactions were performed in CH_3CN–water mixtures at a current density of 1.0 mA cm^{-2} for 10 min. The intermediates using boron-doped diamond as the counter-electrode were further analysed using HRMS.

Theoretical calculations and simulations

EPR spectrum. A direct correlation between changes in A_{iso} (the isotropic hyperfine coupling constant) values of nitrogen-centred radicals and the lone-pair electron configuration on the N nucleus was confirmed in our previous work[46]. We further successfully obtained the Boltzmann conformational distribution of DMPO adducts through molecular dynamics[47,48]. On the basis of the combination of the two techniques, we analyse the EPR spectrum from electrochemical cells. Geometries were optimized using the PBE/6-31++G(d,p)[49] and IEFPCM (Integral Equation Formalism Polarizable Continuum Model) solvent field. Hyperfine coupling constants were obtained using B3LYP/6-31++G, B3LYP/epr-iii and B3LYP/6-311++G(2d,2p) functional level, respectively. All DFT calculations were performed with the Gaussian 16 package[50].

COMSOL Multiphysics simulations. Cell voltage, electric field distribution and proton and ion densities within the vicinity of the electrodes were simulated using COMSOL Multiphysics (https://www.comsol.com/). The electric conductivity of the Ti electrode was taken to be 2.3×10^6 S m^{-1}. Two electrochemical configurations were built to represent the conventional reactor and FRER (Supplementary Fig. 22). For the conventional reactor, the distance between electrodes was set at 20 mm, with the electrolyte containing 4.3 mM NaCl. The electrode model was set with a length of 10 mm and a width of 20 mm. For the FRER, the flow-through mode was set as the mesh structure with several channels, and a velocity of 1.0 mm s^{-1} was applied for further simulation.

The simulation was followed by equations including the Nernst–Planck model and conservation of charge, as well as local

electroneutrality, which represent ion migration caused by the concentration gradient and electrochemical reactions.

$$\frac{\partial c_j}{\partial t} + \nabla \cdot \mathbf{J}_i + \mathbf{u} \cdot \nabla c_j = R_j \quad (1)$$

$$\nabla \cdot \mathbf{i}_l = F \sum_j z_j R_j + F R_{\mathrm{H}} - F R_{\mathrm{OH}} + Q_l \quad (2)$$

$$\sum_j z_j c_j + c_{\mathrm{H}} - c_{\mathrm{OH}} = 0,\ c_{\mathrm{H}} c_{\mathrm{OH}} = K_{\mathrm{w}} \quad (3)$$

where c_j is concentration, $\mathbf{u}$ is velocity, z_j is valence number, $\mathbf{J}_i$ is ionic flux, t represents time, $\mathbf{i}_l$ is the current density of the electrolyte, R_j and Q_l are source terms, K_{w} is the ion product of water and F is the Faraday constant. The diffusion coefficients (D_j) of Na^+, Cl^- and proton were taken to be 2.0×10^{-9}, 1.3×10^{-9} and 7.1×10^{-9} $m^2\ s^{-1}$.

The electrochemical module in COMSOL was used to obtain HER, OER and CER reaction current densities using the Butler–Volmer equation:

$$\mathbf{i}_{\mathrm{loc,expr}} = \mathbf{i}_0 \left(\exp\left(\frac{\alpha_a F \eta}{RT} \right) - \exp\left(\frac{\alpha_c F \eta}{RT} \right) \right) \quad (4)$$

where α_a and α_c are the dimensionless anodic and cathodic charge transfer coefficients, $\mathbf{i}_{\mathrm{loc,expr}}$ is the local charge transfer current density for reaction, $\mathbf{i}_0$ is exchange current density, η is overpotential, R is the universal gas constant and T is temperature, taken to be 293.15 K.

On-site field FRER experiments

The scaled-up experiments were performed in a larger FRER with electrode diameter of 80 mm and designed parallel connection between three cells. The experimental procedures were similar to those of the bench-scale experiments. In contrast to the bench-scale experiments, the brine was the real desulfurization and wastewater from a coal-fired power plant (Anhui, China), and reverse osmosis concentrated wastewater from a coal-chemical industry (Shanxi, China). The brine was presoftened with addition of $Ca(OH)_2$ and Na_2CO_3. A voltage of 3.5 V was applied for field treatment, and a total of 5.0 l of solution was pumped into the tank for 2 h. For comparison, a conventional reactor was used, and all other conditions were kept the same as those of the FRER experiments. TOC was measured using a TOC analyser.

For field experiments, a homemade device was designed by coupling the FRER with ED systems. After reaction for 2 h, as-treated water from the FRER was pumped into the ED system to concentrate the brine. The ED performed in this study was for a 10-cell pair stack, operated in single-pass continuous mode. Each pair was composed of an AEM, a CEM and two spacer channels. Cell pairs were placed in series between the two electrodes, across which a constant external voltage of 10 V was applied. The ED cell consisted of a RuO_2-coated Ti anode, a stainless-steel cathode, an AEM and a CEM (NEOSEPTA CMX, ASTOM). BMED was a special variant of ordinary ED where a bipolar membrane (BM) was inserted between each CEM–AEM pair to form a CEM/BM/AEM assembly. The BMED stack consisted of a RuO_2-coated Ti anode, a stainless-steel cathode, an AEM, a CEM, a BM and spacers. The alkali and metallic impurities were determined using inductively coupled plasma optical emission spectroscopy, which was conducted on an Agilent 730 spectrometer.

The energy consumption in the FRER (EC_{FRER}) was calculated according to the equation

$$\mathrm{EC_{FRER}(kWh\ t^{-1})} = \frac{UIt}{V} \quad (5)$$

where U and I are the voltage and current when the FRER is operating; t is the working time; V is the wastewater volume input at the source.

The energy consumption in ED (EC_{ED}) was calculated according to the equation

$$\mathrm{EC_{ED}(kWh\ t^{-1})} = \frac{U \int_0^t I(t)\,\mathrm{d}t}{V} \quad (6)$$

where $\int_0^t I(t)\,\mathrm{d}t$ is the integration of current over time; V is the wastewater volume input at the FRER source.

The energy consumption in BMED (EC_{BMED}) was calculated according to the equation

$$\mathrm{EC_{BMED}(kWh\ t^{-1})} = \frac{U \int_0^t I(t)\,\mathrm{d}t}{V} \quad (7)$$

where V is the volume of as-concentrated wastewater from ED.

Environmental impact study

LCA work was performed following the ISO standards (ISO 14040/44, 2006). The aim of prospective LCA was to identify key steps in the process chain and assess the environmental impact of FRER-ED. The system boundary for the FRER-ED process included the manufacturing and disposal of electrodes and waste disposal, pollution emission, electricity consumption and by-product utilization. This includes considering the reduction of environmental burdens through the utilization of by-products generated during this process. Moreover, we compared the FRER-ED process with salt crystallization processes to measure the effectiveness of our developed technology. The functional unit was defined as treatment of 1 m^3 of high-salinity wastewater.

A life-cycle inventory was compiled for the ED process as well as the multi-effect evaporation process by including inputs and outputs throughout the entire life cycle. The life-cycle inventory was compiled on the basis of experimental data, literature studies and a commercial database. The inventory of electrode materials was calculated according to preparation processes and service lifetime. The life-cycle inventory of the current salt crystallization processes was carried out by investigating the industry with actual processes.

Gabi 10.5 was employed as the LCA software to calculate the environmental impact of each individual element using the ReCiPe midpoint (H) method. We investigated eight typical impact categories measured using the potential of ecosystem-related categories of climate change (GWP), freshwater ecotoxicity (FETP), terrestrial acidification (TAP) and terrestrial ecotoxicity (TETP), health-related categories of human toxicity (HTP), ozone depletion (ODP) and particulate matter formation (PMFP) and the resource-related category of metal depletion (MDP).

Data availability

All data generated for this study are available in the Article and Supplementary Information. Source experimental data are available from figshare repository at https://doi.org/10.6084/m9.figshare.25390759 (ref. 51).

References

46. Zhao, C., Dao, R., Wang, Y., Yao, J. & Li, H. A DFT investigation exploring the influence of lone electron pair on hyperfine structures of N-centered radicals. *Chem. Phys.* **517**, 13–23 (2019).
47. Houriez, C., Ferre, N., Siri, D., Tordo, P. & Masella, M. Assessing the accuracy of a QM/MM//MD combined protocol to compute spectromagnetic properties of polyfunctional nitroxides in solution. *Theor. Chem. Acc.* **131**, 1240 (2012).
48. Yamaguchi, M. DFT calculation of isotropic hyperfine coupling constants of spin adducts of 5,5-dimethyl-1-pyrroline-*N*-oxide in benzene and water. *Comput. Theor. Chem.* **1104**, 24–31 (2017).
49. Cohen, A. J., Mori-Sánchez, P. & Yang, W. Challenges for density functional theory. *Chem. Rev.* **112**, 289–320 (2012).

50. Gaussian 16 rev. C.01 (Gaussian, Inc., 2016).
51. Zhang, G. & Liu, H. Source data for "Redox-neutral electrochemical decontamination of hypersaline wastewater with high technology readiness level". *figshare* https://doi.org/10.6084/m9.figshare.25390759 (2024).

Acknowledgements

We acknowledge the National Natural Science Foundation of China (grants 52221004 to H.L., 22022606 to G. Zhang), X. Li and J. Lin from Beijing Capital Eco-Environment Protection Group Co., Ltd. for supporting this project and M.Z. Li from Huaibei GO-ON Power Co., Ltd. for supporting our field experiment. We thank Q. Liu from the Department of Chemistry, Tsinghua University, for discussions on the mechanisms of catalysis and electrochemical measurements. We also thank S. Qu from Beijing Institute of Technology for supporting LCA analysis. We thank A.L. Chun of Science Storylab for critically reading and editing the paper.

Author contributions

H.L. directed the project. G. Zhang designed the experiments. G. Zhang and Y.L. synthesized the materials and performed the bench-scale degradation and electrochemical experiments. G. Zhang and C.Z. analysed results of in situ EPR experiments. J.G., Y.L. and Q.C. performed the on-site field experiments. G. Zhou carried out the DFT calculations. W.-J.F. and Y.L. collected and analysed the HRMS data. Q.Z. and Y.L. conducted the LCA analysis. G. Zhang, Y.S., Y.L. and H.L. co-wrote the Article. H.L., Q.J., F.X. and J.Q. revised the Article. All authors discussed the results and commented on the Article.

Competing interests

The authors declare no competing interests.

Additional information

Supplementary information The online version contains supplementary material available at https://doi.org/10.1038/s41565-024-01669-3.

Correspondence and requests for materials should be addressed to Huijuan Liu.

Peer review information *Nature Nanotechnology* thanks Yang Yang and the other, anonymous, reviewer(s) for their contribution to the peer review of this work.